PCCP

ROYAL SOCIETY OF CHEMISTRY

PAPER

View Article Online
View Journal | View Issue



Cite this: *Phys. Chem. Chem. Phys.*, 2020, **22**, 15608

# Internal conversion and intersystem crossing dynamics of uracil upon double thionation: a time-resolved photoelectron spectroscopy study in the gas phase†

Abed Mohamadzade and Susanne Ullrich *

Received 22nd April 2020,
Accepted 24th June 2020

DOI: 10.1039/d0cp02145h

rsc.li/pccp

The photophysical properties of 2,4-dithiouracil (2,4-DTU) in the gas phase are studied by time-resolved photoelectron spectroscopy (TRPES) with three different excitation wavelengths in direct extension of previous work on uracil (U), 2-thiouracil (2-TU) and 4-thiouracil (4-TU). Non-radiative deactivation in the canonical nucleobases like uracil mainly occurs *via* internal conversion (IC) along singlet excited states, although intersystem crossing (ISC) to a long-lived triplet state was confirmed to play a minor role. In thionated uracils, ISC to the triplet state becomes ultrafast and highly efficient with a quantum yield near unity; however, the lifetime of the triplet state is strongly dependent on the position of the sulfur atom. In 2-TU, ISC back to the ground state occurs within a few hundred picoseconds, whereas the population remains trapped in the lowest triplet state in the case of 4-TU. Upon doubling the degree of thionation, ISC remains highly efficient and dominates the photophysics of 2,4-DTU. However, several low-lying excited states contribute to competing IC and ISC pathways and a complex deactivation mechanism, which is evaluated here based on TRPES measurements and discussed in the context of the singly thionated uracils.



## Introduction

Thiobases are a class of modified nucleobases with sulfur replacing an oxygen atom in an exocyclic carbonyl group.[1,2] Such sulfur-containing nucleosides naturally occur in transfer RNA, which links the messenger RNA and protein information systems and helps assemble amino acids into a functional sequence.[3] Furthermore, thiobases serve as photosensitizers for pharmacological applications like photodynamic therapies.[4–8] These benefit from red-shifted absorption spectra of the thiobases which allow selective excitation at longer wavelengths of light that penetrate deeper into the tissue.[9–11] Most importantly, intersystem crossing outcompetes internal conversion, and reactive triplet states are generated with high quantum yields.[6,12–19] Therapeutic action, *e.g.*, for cancer treatments, subsequently occurs *via* generation of reactive singlet oxygen species or direct crosslinking reactions.[20,21] Consequently, an extended triplet lifetime, as observed in some thiobases, enhances these processes and translates into the efficacy of these drugs.

The thiobases are also intriguing from a fundamental photochemical point of view. Despite their similarity to the canonical nucleobases, their photodynamics are surprisingly different.[11,13,22–28] Exploring such structure-dynamics relationships in thiobases has therefore been the subject of several experimental[6,11,13–16,22–25,29–32] and theoretical[12–18,22,24,33–37] studies, but among the extensive literature, the number of gas-phase spectroscopy experiments[22–25,38] currently remains very limited. In an extension of these previous works, the focus here is on thiouracils.

There is general agreement in the literature that UV photoexcited uracil (U) undergoes highly efficient internal conversion (IC) back to the ground state, and only a minor fraction intersystem crosses (ISC) into a long-lived triplet state.[25] Upon thionation, the conical intersections (CI) that connect the singlet excited states to the ground state become energetically inaccessible, which drastically alters the photodynamics. Following photoexcitation to the bright $^1\pi\pi^*$ state, initially 2-thiouracil (2-TU) and 4-thiouracil (4-TU) also deactivate to the lower-lying dark $^1n\pi^*$ state.[39] In contrast to uracil, intersystem crossing close to the $^1n\pi^*$ minimum, facilitated by higher spin–orbit coupling, populates the triplet manifold with quantum yields close to unity. However, intricate details of the potential energy surface topography lead to a surprising dependence of the intersystem crossing dynamics on the position of

*Department of Physics and Astronomy, University of Georgia, Athens, GA 30602, USA. E-mail: ullrich@uga.edu*

† Electronic supplementary information (ESI) available: The fitting procedure, equations and additional fitting results are discussed in more detail. See DOI: 10.1039/d0cp02145h

the sulfur atom. When comparing 2-TU and 4-TU after excitation at the maximum of their first absorption band, 2-TU intersystem crosses to the triplet manifold in 544 fs and subsequently back to the ground state in 142 ps. In stark contrast, intersystem crossing takes 2.66 ps in 4-TU and is followed by extended ($>$1.5 ns) trapping in the lowest triplet state.[22,23,25]

These observations motivated the Time-Resolved Photoelectron Spectroscopy (TRPES) study on 2,4-dithiouracil (2,4-DTU) presented here, which investigate how double-thionation, *i.e.*, simultaneous thionation of both the 2- and 4-positions, affects the photodynamics. The differential nature of TRPES makes it an ideal choice for disentangling convoluted photophysical pathways involving optically dark states. The technique simultaneously provides dynamics and spectral information that allows identification of electronically excited states and monitors the evolution of the population dynamics between them. Furthermore, gas-phase spectroscopy studies intrinsic molecular properties free from external perturbations, *i.e.*, the solvent environment, and hence experimental observations are directly comparable to *ab initio* calculations and dynamics simulations.

## Experimental details

More details on the experimental set-up can be found in ref. 40–42. Briefly, the TRPES experiment consists of two different parts—a gaseous molecular beam spectrometer and a femtosecond laser system with UV conversion capabilities. The first part is equipped with a magnetic bottle-type photoelectron kinetic energy analyzer. The latter consists of a diode-pumped Ti:Sa oscillator (MIRA Optima 900) and a regenerative amplifier (Legend Elite HE) with 802 nm output at 1 kHz repetition rate which pumps a Traveling-Wave Optical Parametric Amplifier (TOPAS-C).

Pump pulses generated by the TOPAS are tuned to three different wavelengths across the first absorption band of 2,4-DTU; 344.3 and 361.4 nm correspond to the rising edge and maximum of the band, whereas 376 nm excites in an overlap region with contributions from the second absorption band. The second harmonic of the amplifier fundamental (401 nm) serves as a probe and is time delayed relative to the pump *via* an electronically controlled, motorized optical delay line. This probe wavelength is below the onset of the absorption spectrum and chosen to minimize unwanted probe–pump signals. Since one-photon excitation but two-photon ionization is desired, the pulse energy is set to 2.2–3 μJ for the pump and 13–14 μJ for the probe. This $1 + 2'$ multiphoton process is confirmed experimentally, given that the total photon energy of $1 + 1'$ is insufficient for ionization and $1 + 3'$ processes would result in photoelectrons of significantly higher kinetic energies. Pump and probe pulses are focused by two separate 50 cm lenses and are overlapped spatially at a small angle inside the molecular gas beam within the ionization region of the spectrometer. 2,4-DTU powder from Sigma-Aldrich (98%) is held inside a quartz sample holder and heated to 150–180 °C. The evaporated molecules are co-expanded continuously with a Helium carrier gas and transferred into the photoelectron spectrometer by the molecular beam *via* an intermediate differential pumping stage.

The 2D TRPES spectra are derived from photoelectron time-of-flight (TOF) measurements at various pump–probe delays. In order to accurately capture the ultrafast dynamics as well as extended decay components, each scan is recorded with an equal step size of 25 fs over the pump–probe range from −1 to 4 ps followed by unequal, gradually increasing steps up to a maximum delay of 300 ps. In addition to averaging 4000 shots at each pump–probe delay, the delay stage scans four sweeps back and forth in order to eliminate any potential signal instabilities due to slow drifts in molecular beam intensity or laser pulse energies. Furthermore, one-color signals are recorded throughout the scan by use of shutters for dynamic background subtraction. A Labview based data acquisition program incorporating a multiscalar TOF readout handles the measurement sequence and instrument control. The measured photoelectron TOF spectra are converted to electron kinetic energies using calibration constants acquired through TRPES measurements on 1,3 butadiene (BD) with known energies of cationic vibrational levels.[43] The BD scans simultaneously serve for timing calibrations, *i.e.*, the position of zero pump–probe delay (time zero) and instrument response function (time resolution). For all pump wavelengths, a Gaussian full-width-at-half-maximum (FWHM) of approximately ∼180 fs was determined.

The TRPES spectra are analyzed by fitting sequential exponential decay dynamics to the integrated photoelectron signals as well as global lifetime analysis of the 2D data. The latter technique primarily served for analysis of the truncated TRPES data set to characterize prominent spectral changes that occur within the first 3.75 ps after excitation. A long-lived (nanosecond) component, which is extracted separately from a fit to the integrated time-trace of the long-range TRPES scan, is kept fixed during the 2D analysis. Overall, a three-step sequential decay was determined to describe the data best, although a fourth exponential was needed to account for a small probe–pump contribution toward negative delays. All exponential fitting functions were convoluted with the Gaussian cross-correlation with parameters obtained from the timing calibration. Further details regarding the fitting procedure, equation, as well as additional fitting results, are provided in the ESI.†

## Discussion

### Absorption spectrum

The chemical structure of the lowest energy dithione tautomeric form of 2,4-DTU is shown as an inset in Fig. 1(a). The dithiol and four keto-thione forms (see ESI†) are destabilized by 28 kJ mol$^{-1}$ or more and therefore considered negligible under molecular beam conditions.[17,19,44]

Since no gas-phase absorption spectrum of 2,4-DTU has been reported in the literature yet, the solution-phase spectrum of 2,4-DTU dissolved in carbon tetrachloride (CCl4) in Fig. 1(a) is used for reference instead. CCl4, which is a non-polar

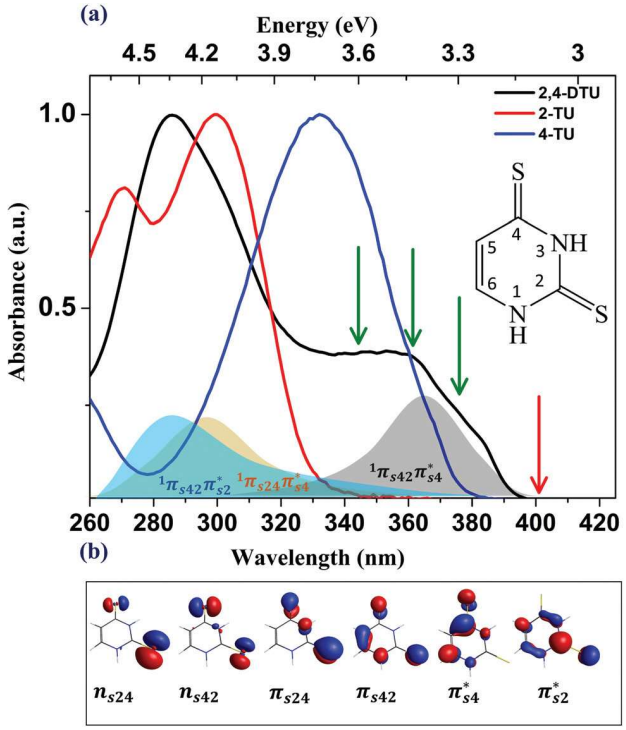


Fig. 1 (a) Normalized absorption spectra of 2,4-DTU, 4-TU and 2-TU recorded in carbon-tetrachloride solution as a function of wavelength and its energy equivalent (bottom and top *X*-axis, respectively). The underlying electronic transitions contributing to the first absorption band of 2,4-DTU are based on ref. 45. Green arrows represent the pump wavelengths, while the red arrow indicates the probe. The inset shows the chemical structure 2,4-DTU in its dominant dithione form with atomic numberings. (b) Calculated orbitals configurations using the unrestricted Hartree–Fock method in GAMESS for the ground state geometry by ref. 46–48. These orbitals are meant for visualization only.

solvent, can be considered a good approximation of a gas-phase environment as justified by way of comparison to calculated transition energies and absorption spectra. According to Leszczynski *et al.*,[19] the four lowest bright $\pi \rightarrow \pi^*$ transition energies show energetic shifts less than 0.2 eV upon solvation in much more polar solvents such as acetonitrile and water. Oscillator strengths and hence relative band intensities, on the other hand, show a strong solvent dependence and the absorption spectrum in Fig. 1(a) most closely resembles the overall shape of calculated gas-phase spectra.[19,34,45] Specifically, in the gas phase as well as CCl4 2,4-DTU spectra, the first band, relative to the second, appears weaker. To visualize shifts in the absorption bands upon thionation, and facilitate the discussion of underlying orbital transitions, the spectra of 2-TU and 4-TU in CCl4 are also included in Fig. 1(a).

The 2,4-DTU absorption spectrum has an onset around 397 nm (3.12 eV) and two distinct maxima at around 360 nm (3.44 eV) and 286 nm (4.33 eV), which occur at similar energies as the lowest bands in 4-TU and 2-TU, respectively. Generally speaking, in these singly thionated uracils, the lowest bright transition involves $\pi$ and $\pi^*$ orbitals of the aromatic ring but also with significant participation from the thiocarbonyl bond.[11,22,23,45,49] For 2,4-DTU assignment of an electronic state character is less clear due to the presence of two sulfur atoms, which leads to mixed orbital contributions. Furthermore, eight electronically excited states are predicted below 5 eV including four that are bright in absorption and four dark states embedded within them.[19,34] The most relevant state assignments for the first absorption band of the 2,4-DTU spectrum are visualized in Fig. 1(a) with the associated orbitals in Fig. 1(b). The nomenclature used here is meant to be descriptive of the orbital contributions on the sulfur atoms. For example, a subscript S2 specifies that an orbital is localized mostly on the sulfur in position 2 (*i.e.*, electron density on S4 negligible), whereas S24 indicates orbitals on each of the sulfur atoms but with more charge distribution on position 2 than 4. While $n \rightarrow \pi^*$ transitions originate from orbitals that are almost entirely localized on the sulfur atoms, it should be noted that all $\pi \rightarrow \pi^*$ transitions also involve aromatic ring orbitals. The first absorption band at 360 nm is mainly associated with a transition to the singlet $^1\pi_{s42}\pi_{s4}^*$ state with minor but increasing contributions from higher excited states, $^1\pi_{s42}\pi_{s2}^*$ and $^1\pi_{s24}\pi_{s4}^*$, toward shorter wavelengths. These latter states are also responsible for the second and more intense band around 286 nm which is not studied in this work. Additionally, four $n \rightarrow \pi^*$ transitions extend over the wavelength range from 250 to 400 nm, but with close to zero intensities,[34,45,49] which involve excitations from the sulfur lone-pair orbitals to the $\pi_{s2}^*$ or $\pi_{s4}^*$ orbitals.

The large number of low-lying singlet and triplet excited states associated with the orbital transitions discussed above contribute to potentially complex photophysics in 2,4-DTU, including competitions between various internal conversion and intersystem crossing processes. The photoexcitation wavelengths for this study were therefore selected to coincide with the first absorption band (see Fig. 1) and predominantly populate the lowest bright state, $^1\pi_{s42}\pi_{s4}^*$. By increasing the amount of vibrational excitation, further insights into barriers along the deactivation pathways and accessibility of conical intersections may be gained. Fig. 1(a) also indicates increasing contributions from higher-lying electronic excited states to the photoexcitation process. Both scenarios will result in a wavelength-dependency of the pathways and lifetimes of the involved, intermediate states that are evaluated in the analysis below.

### Analysis of time-resolved photoelectron spectra

Fig. 2 shows the 2,4-DTU TRPES results in the order of decreasing excitation wavelength from the top row to bottom. For more clarity of the fast dynamics, the 2D spectra (column 1) are abbreviated to a maximum pump–probe delay of ~3.75 ps and plotted as a function of electron binding energy (eV) to facilitate direct comparison to calculated ionization potentials. Electron binding energies are calculated by subtraction of the measured photoelectron kinetic energy from the total photon energy ($1 + 2'$); the high binding energy cut off corresponds to the total photon energy. The steep drop in photoelectron signal near the cut off is due to the low collection efficiency of the magnetic bottle for near-zero kinetic energy electrons and hence not necessarily an inherent spectroscopic feature of the

 

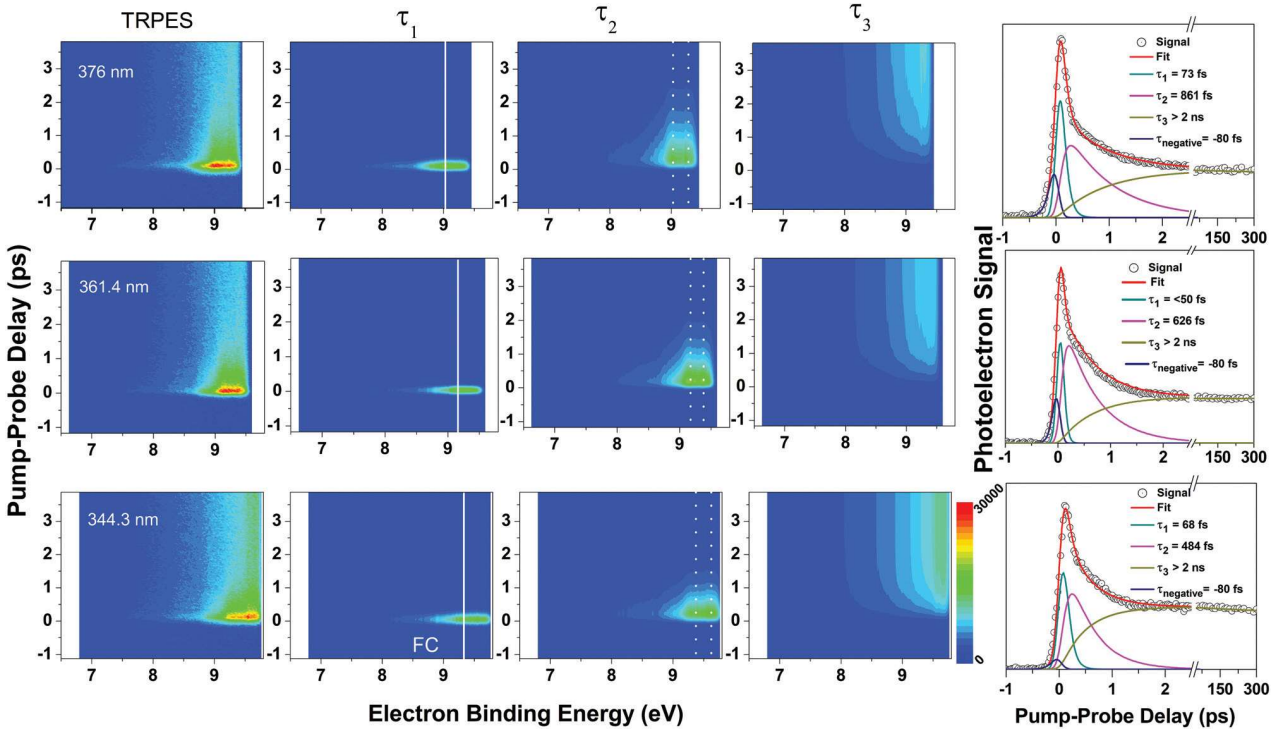


Fig. 2 The experimental TRPES data for three different pump wavelengths, in decreasing order from top to bottom, is displayed in the first column. 2D maps represent photoelectron spectra plotted in electron binding energy (eV) along the *X*-axis *versus* the pump–probe delay time (ps) on *Y*-axis. The photoelectron yield at a specific energy and delay is indicated by the color scheme with blue corresponding to zero and red to the maximum signal. The signal levels of the color scheme are maintained in column 2–4 for the individual pump–probe decay components extracted from global lifetime analysis (sequential model) and kept similar for the different excitation wavelengths. Additional fit results including 2D maps of the total fit, residuals, and probe–pump contribution are provided in the ESI.† Column 5 shows time-traces of the photoelectron yield (signal), fit and contributions of each decay component which were obtained by integration of the respective 2D maps over all electron binding energies. The solid white lines in column 2 indicate an expected position of the photoelectron band within the Franck–Condon region calculated based on the *ab initio* ground state photoelectron spectrum by Ruckenbauer *et al.*[17] and an estimated shift due to excitation wavelengths dependent on vibrational excitation. The dotted lines in column 3 mark the experimentally observed double-peak structure in the intermediate component of the TRPES spectra.

molecule. 2D global lifetime analysis, *i.e.* the simultaneous fit of sequential decay time constants and spectra, yields the individual 2D contributions plotted in columns 2–4. Column 5 shows the energy-integrated time traces (*i.e.*, photoelectron yields) over the entire pump–probe delay range of the TRPES scan along with time traces of the individual contributions and their associated decay times. A fourth, negative exponential decay accounts for unwanted, minor contributions from probe–pump processes. This is attributed to two-photon photoexcitation with the 400 nm probe followed by one-photon ionization with the pump. Table 1 summarizes only the pump–probe time constants that are of relevance to the discussion of the 2,4-DTU photodynamics. The probe–pump time constant ($\tau_{neg} = -80$ fs) is identical in all three TRPES given that the dynamics are initiated by the same 2 × 400 nm photoexcitation.

Table 1 Time-constants extracted based on a three-step sequential exponential decay model. A fourth negative decay component around 80 fs is needed to account for probe–pump contributions. The relative error on the fit is reported for the first and second time-constants

| Pump wavelength (nm) | Pump energy (eV) | $\tau_1$ (fs) | $\tau_2$ (fs) | $\tau_3$ (ns) |
|---|---|---|---|---|
| 376 | 3.30 | 73 ± 25 | 861 ± 50 | >2 |
| 361.4 | 3.43 | <50 | 626 ± 50 | >2 |
| 344.3 | 3.60 | 68 ± 25 | 484 ± 50 | >2 |

Further analysis of the TRPES spectra, in particular, assignment of the spectral contributions in columns 2–4, benefits from theoretical support. Although *ab initio* non-radiative excited-state deactivation pathways for 2,4-DTU in solution have recently been reported,[50] solvent effects are expected to perturb the decay mechanism.[12,22] In the absence of similar calculations for the gas phase, a model for the deactivation in isolated 2,4-dithiothymine (2,4-DTT) by Cui *et al.*[12] provides valuable guidance. Additionally, information on the cationic states is available from theoretical photoelectron spectra for ground state ionization of 2,4-DTU by Ruckenbauer *et al.*[17] The calculated photoelectron spectra reveal two ionization bands in the 8–10 eV range and around 12 eV. The latter, which is associated with ionization of orbitals localized on the pyrimidine ring, is energetically inaccessible with the total photon energies in the TRPES experiments and, therefore, not discussed further. The first band shows a double peak structure composed of four ionization channels, $S_0 \rightarrow D_{0-3}$. The dominant contributions are characterized as an n-hole on S4 for $D_0$

(8.74 eV), n-hole on S2 for $D_3$ (9.14 eV), and π-holes that involve both sulphur atoms, S2 and S4, for $D_1$ (8.86 eV) and $D_2$ (9.02 eV).[17] Based on these cationic orbital assignments, ionization preferences from electronically excited states are derived for interpretation of the TRPES spectral contributions. In contrast to the cationic states, which show a significant degree of orbital localization on the Sulphur atoms, electronic excitation is generally more delocalized over sulphur and ring orbitals. Considering that in 2,4-DTU orbitals on both sulphur atoms participate in electronic transitions, generally nπ* states are expected to ionize into the n-holes, $D_0$ and $D_3$, whereas ππ* states correlate with the π-holes, $D_1$ and $D_2$. Specifically: $^1\pi_{s42}\pi_{s4}^*$, $^1\pi_{s42}\pi_{s2}^* \rightarrow D_1$; $^1\pi_{s24}\pi_{s2}^* \rightarrow D_2$; $^1n_{s42}\pi_{s4}^* \rightarrow D_0$; $^1n_{s24}\pi_{s2}^* \rightarrow D_3$. Identical correlations are to be expected for the corresponding triplet states. The calculated photoelectron spectra by Ruckenbauer *et al.*[17] are static and only describe ionization at the ground state geometry, and this limits a comparison to the TRPES spectra directly after photoexcitation, *i.e.*, for ionization within the Franck–Condon region. At longer pump–probe delays, the *ab initio* pathways in 2,4-DTT calculated by Cui *et al.*[12] become relevant to data analysis and interpretation. 2,4-DTT differs from 2,4-DTU only by an additional methyl group in the C5 position and, due to the similarity of their electronic structures, an analogous relaxation mechanism is expected for 2,4-DTU. This assumption can be justified on the basis of a previous experimental and theoretical study comparing uracil and thymine.[51] It showed that the nonpolar methyl group minimally perturbs the excited-state deactivation pathway, although relaxation times associated with the out-of-plane motion of the heavier substituent increase. Similar effects are expected when considering 2,4-DTU and 2,4-DTT. Furthermore, *ab initio* calculations show that electronic transition energies of the lowest six excited states are mostly unaffected by methylation and the ordering and electronic character is preserved.[12,19] This provides additional justification for considering the 2,4-DTT theoretical pathways as guidance for assignment of our 2,4-DTU TRPES spectra.

### Deactivation pathway and dynamics

The six low-lying excited states contribute to the complexity of the deactivation mechanism,[12] which is visualized in Fig. S4 in the ESI.† Common to all three pathways is the internal conversion from the initially photoexcited $^1\pi_{s42}\pi_{s4}^*$ state to a four-state intersection; furthermore, the final state, that all pathways relax to, is the minimum of the lowest triplet state, $^3\pi_{s24}\pi_{s4}^*$. The pathway indicated by solid lines is expected to dominate the photodynamics of 2,4-DTT. The close proximity of the $^1n_{s24}\pi_{s2}^*$ minimum and three other excited states ($^3\pi_{s42}\pi_{s2}^*$, $^3n_{s42}\pi_{s4}^*$, $^1n_{s42}\pi_{s4}^*$) results in a quasi four-state intersection, but IC to the lowest singlet excited state, $^1n_{s42}\pi_{s4}^*$, is considered more efficient than ISC into the triplet manifold (either $^3\pi_{s42}\pi_{s2}^*$ or $^3n_{s42}\pi_{s4}^*$). The $^1n_{s42}\pi_{s4}^*$ then depopulates *via* ISC to the lowest triplet state, $^3\pi_{s24}\pi_{s4}^*$.

**Internal conversion ($\tau_1$).** By starting with a visual inspection of 2D spectra (Fig. 2 columns 1–4), all look similar except for a general shift towards higher electron binding energies at shorter excitation wavelengths. This is associated with increasing vibrational excitation as more photon energy is deposited into the molecule. Estimating an experimental value for the $^1\pi_{s42}\pi_{s4}^*$ minimum from the onset of the absorption spectrum, which is around 397 nm (3.12 eV), pumping the molecule with 376 nm (3.3 eV), 361.4 nm (3.43 eV), and 344.3 nm (3.6 eV) results in up to 0.18, 0.31 and 0.48 eV vibrational excitation of this state, respectively. During photoionization, excess vibrational excitation is transitioned to the cation. In the Franck–Condon region, *i.e.*, at short pump–probe delays, a direct comparison to the ground-state photoelectron spectra by Ruckenbauer *et al.*[17] can be made. The experimental photoelectron band for ionization from $^1\pi_{s42}\pi_{s4}^*$ would be expected at an electron binding energy corresponding to the calculated $D_1$ (8.859 eV)[17] plus a wavelengths-dependent vibrational excitation. The white lines labeled FC in Fig. 2, column 2 indicate these predicted values. The excellent agreement between prediction and observation lends support for the assignment of the photoelectron signal in column 2 to the lowest bright $^1\pi_{s42}\pi_{s4}^*$ as the initially excited state, although high-lying ππ* states, such as the $^1\pi_{s42}\pi_{s2}^*$ and $^1\pi_{s24}\pi_{s4}^*$ may participate to a lesser extent. Two factors contribute to the broadness of the observed photoelectron signal. Ionization from the sulphur localized π-orbitals into $D_1$ and $D_2$ leads to two overlapping features with peaks positioned at 8.86 eV and 9.02 eV, respectively.[17] These are unresolved in the experiment due to ultrafast excited-state relaxation out of the FC region towards the $^1\pi_{s42}\pi_{s4}^*$ minimum, which has been associated with an increase in ionization potential and gain in vibrational kinetic energy.[22,23] Furthermore, a tail extends toward lower electron binding energies, and its onset coincides with the experimental adiabatic ionization potential of 8.36 eV reported by ref. 17. However, the signal intensity is weak due to unfavorable ionization correlations and vibrational overlap between excited and cationic states. The $^1\pi_{s42}\pi_{s4}^*$ state decays on an ultrafast timescale, $\tau_1$, provided in Table 1. Internal conversion, as opposed to intersystem crossing, is considered more likely for a process that occurs on tens of femtoseconds. Hence, the photoelectron signal in column 3 is attributed to lower-lying singlet excited states, with $^1n_{s24}\pi_{s2}^*$ and $^1n_{s42}\pi_{s4}^*$ as potential candidates based on theoretical predictions.[12,45] For 2,4-DTT,[12] internal conversion from the $^1\pi_{s42}\pi_{s4}^*$ along two parallel paths populates the $^1n_{s24}\pi_{s2}^*$ state which is linked to the $^1n_{s42}\pi_{s4}^*$ *via* a four-state quasi degeneracy.

Close visual inspection of the component in column 3 reveals a slight double-peak structure in the experimental photoelectron spectrum of 2,4-DTU; two dotted, white lines indicate the individual peak positions. For nπ* states the nonbonding orbitals are mostly localized on both Sulphur atoms in either symmetric or antisymmetric configuration and, hence, preferential ionization of the $^1n_{s24}\pi_{s2}^*$ state into $D_3$ and $^1n_{s42}\pi_{s4}^*$ into $D_0$ are to be expected.[17] Considering that the calculated photoelectron spectra show a separation of 0.40 eV between $D_0$ and $D_3$, as opposed to 0.16 eV between $D_1$ and $D_2$, features from ionization of nπ* states may appear more distinguishable than in the case of ππ* states. Conversely, mixing

 

of the nπ* states, as predicted by certain levels of theory,[34] leads to sharing of the ionization channels which prevents a deconvolution of the $^1n_{s24}\pi_{s2}$* and $^1n_{s42}\pi_{s4}$* dynamics. To account for the observed double-peak structure, the photoelectron spectrum in column 3 is associated with the observation of both $^1$nπ* states.

**Intersystem crossing ($\tau_2$) and triplet state trapping ($\tau_3$).** The lower $^1n_{s42}\pi_{s4}$*, which is also the lowest singlet excited state, provides access to intersystem crossing into the triplet manifold and is described by time-constant $\tau_2$ in Table 1. Although intersystem crossing from the higher $^1n_{s24}\pi_{s2}$* to the $^3\pi_{s42}\pi_{s2}$* and $^3n_{s42}\pi_{s4}$* *via* the four-state intersection are energetically possible these processes are less efficient than internal conversion, and the latter additionally violates El-Sayed's rule.[52]

Column 4 represents a long (>ns) component, which is assigned to the lowest-lying triplet $^3\pi_{s24}\pi_{s4}$* state and its decay back to the ground state. Regardless of the pathway that led to the population of the $^3\pi_{s24}\pi_{s4}$* minimum, extended trapping due to spin forbidden deactivation back to the ground state and a high barrier to access the crossing point[53] provides strong evidence for an unambiguous assignment. Similar to 2-TU and 4-TU, little to no shift in the photoelectron spectrum is observed during the intersystem crossing from the lowest $^1$nπ* to the triplet state. Unfortunately, lack of excited and cationic state *ab initio* calculations prevents a more quantitative analysis of this photoelectron band to support this assignment.

**Excitation wavelength-dependency of dynamics.** In summary, the photoelectron spectra confirm a photophysical model, visualized in Fig. 3, that involves multi-step internal conversion from an initially excited $^1\pi\pi^*$ state, *via* the $^1n_{s24}\pi_{s2}$* intermediate, to the lowest $^1n_{s42}\pi_{s4}$* state followed by intersystem crossing and extended trapping in the lowest triplet state, $^3\pi_{s24}\pi_{s4}$*. Further details on the deactivation paths can be derived from the wavelengths-dependencies of the time constants in Table 1. For example, a decrease in time constants at shorter excitation wavelengths is generally characteristic of the presence of barriers along pathways. Excess vibrational excitation aids with overcoming these barriers in order to access the (conical) intersections that promote internal conversion and intersystem crossing to the lower-lying potential energy surfaces. For example in 2,4-DTT, *ab initio* calculations have predicted the $^1\pi_{s42}\pi_{s4}$*/$^1n_{s24}\pi_{s2}$* conical intersection 0.2 eV above the $^1\pi_{s42}\pi_{s4}$* state minimum,[12] which explains faster dynamics following 361.4 nm compared to 376 nm excitation for the first internal conversion step ($\tau_1$). Although an increase in time constant $\tau_1$ at 344.3 nm excitation appears to contradict such a trend, in reference to Fig. 1, this can easily be explained by initial photoexcitation of the higher-lying $^1\pi_{s42}\pi_{s2}$* and $^1\pi_{s24}\pi_{s4}$* states which subsequently populate the $^1\pi_{s42}\pi_{s4}$* state. This additional, ultrafast internal conversion step cannot be resolved in the TRPES measurement but instead is observed as an apparent increase in time-constant $\tau_1$. Fig. 3 omits the non-radiative decay pathways from the higher $^1\pi\pi^*$ states for simplicity. On the other hand, calculations predict the $^1n_{s42}\pi_{s4}$*/$^3\pi_{s24}\pi_{s4}$* crossing close to the $^1n_{s42}\pi_{s4}$* minimum[12] although a clear trend in time constant $\tau_2$ in the experiment suggests the presence of a small barrier.

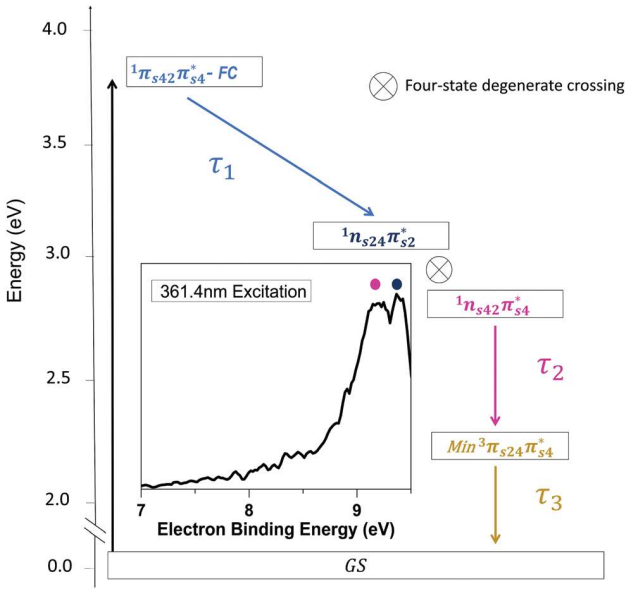


Fig. 3 Proposed deactivation pathway for photoexcited 2,4-DTU. The model is based on TRPES experimental data guided by *ab initio* calculations for 2,4-DTT.[12] The excited state minima and proposed four state intersection are placed according to their calculated energies. The double peak structure (colored circles) of the photoelectron spectrum at ~300 fs provides experimental evidence for the involvement of both singlet $^1$nπ* states in the intersystem crossing process to the lowest triplet state.

## Comparison to singly substituted uracils

In comparing the 2,4-DTU photodynamics to the singly thionated species following photoexcitation at their respective absorption maxima, it becomes apparent that in this class of molecules, the lowest singlet $^1$nπ* state provides an access point to the triplet manifold. In all three molecules, the $^1$nπ* is populated *via* internal conversion within <75 fs. Dissimilarities are however observed in the intersystem crossing dynamics. Both 2-TU and 2,4-DTU undergo intersystem crossing within a few hundred femtoseconds, whereas in 4-TU, the process takes several picoseconds. The singly thionated species undergo intersystem crossing close to the $^1$nπ* minimum but the spin–orbit coupling to the triplet manifold is larger in 2-TU (275 $cm^{-1}$) than in 4-TU (157 $cm^{-1}$).[22–24] The observation here may imply that similar to 2-TU, high spin–orbit-coupling causes ultrafast intersystem crossing in 2,4-DTU. Stark differences in ground state repopulation are associated with barriers to access the $S_0$ crossing point from the triplet state minimum.[53] In 2-TU, this amounts to 0.2 eV compared to 0.72 eV in 4-TU. Hence, in the case of the 4-TU population is trapped in the lowest triplet state and similar reasoning may be applied to 2,4-DTU. In the absence of *ab initio* potential energy surfaces for 2,4-DTU, this remains somewhat tentative but is consistent with predictions for substituted thiothymines.[53]

A comparison to solution-phase photodynamics is only possible to a limited extend. In general, 2,4-DTU in solution undergoes similar ultrafast (few hundred femtosecond) ISC to a long-lived triplet state. Whether this process occurs directly from the photoexcited bright $^1\pi\pi^*$ state or *via* a dark $^1$nπ* intermediate

is still under debate.[50] Given that states of $n\pi^*$ and $\pi\pi^*$ character are affected differently by the solvent environment, their relative energetic shifts will lead to changes in intricate details of the potential energy surfaces, including barriers and intersections, which govern the relaxation pathways.[12,19]

## Conclusions

A model for the photodynamics of 2,4-DTU was derived from experiments employing gas-phase time-resolved photoelectron spectroscopy and is shown in Fig. 3. The proposed deactivation pathway is discussed in the context of *ab initio* calculations on related thiobases such as 2,4-DTT and singly thionated uracils, 2-TU and 4-TU.

Photoexcitation of the first absorption band primarily occurs into the $^1\pi_{s42}\pi_{s4}^*$ excited state although two higher-lying $^1\pi\pi^*$ states may contribute at shorter wavelengths. This is followed by immediate motion out of the Franck–Condon region and ultrafast internal conversion into the minimum of the singlet excited $^1n_{s24}\pi_{s2}^*$ state, which, according to calculations, forms a four-state intersection with three other degenerate states ($^3\pi_{s42}\pi_{s2}^*$, $^3n_{s42}\pi_{s4}^*$, $^1n_{s42}\pi_{s4}^*$). From there, internal conversion to the lower singlet $^1n_{s42}\pi_{s4}^*$ state is observed as evidenced in a double peak structure in the associated photoelectron spectrum. Subsequent intersystem crossing into the lowest triplet state, $^3\pi_{s24}\pi_{s4}^*$ occurs on sub-picosecond timescales, and the molecule remains trapped in the state minimum beyond the time range of the experiment. Generally, time constants were observed to decrease at shorter photoexcitation wavelengths. This trend is indicative of barriers along the deactivation pathway that are more easily surmounted with an increase in excess vibrational excitation.

## Conflicts of interest

There are no conflicts to declare.

## Acknowledgements

This work was supported by the National Science Foundation grant CHE-1800050.

## References

1 B. Ashwood, M. Pollum and C. E. Crespo-Hernández, *Photochem. Photobiol.*, 2019, **95**, 33–58.
2 S. Arslancan, L. Martínez-Fernández and I. Corral, *Molecules*, 2017, **22**, 998.
3 W. Saenger, *Principles of nucleic acid structure*, Springer, New York, 1984, pp. 1–8.
4 C. E. Crespo-Hernandez and M. Pollum, *US Pat.*, 10413608, 2019.
5 M. Pollum, L. Martínez-Fernández and C. E. Crespo-Hernández, *Photoinduced phenomena in nucleic acids I*, Springer, 2014, pp. 245–327.
6 M. Pollum, S. Jockusch and C. E. Crespo-Hernández, *J. Am. Chem. Soc.*, 2014, **136**, 17930–17933.
7 M. Pollum, M. Lam, S. Jockusch and C. E. Crespo-Hernández, *ChemMedChem*, 2018, **13**, 1044–1050.
8 E. Gemenetzidis, O. Shavorskaya, Y.-Z. Xu and G. Trigiante, *J. Dermatol. Treat.*, 2013, **24**, 209–214.
9 R. Singh and R. Yadav, *Spectrochim. Acta, Part A*, 2014, **130**, 188–197.
10 A. L. Appleton, S. M. Brombosz, S. Barlow, J. S. Sears, J.-L. Bredas, S. R. Marder and U. H. Bunz, *Nat. Commun.*, 2010, **1**, 91.
11 M. Pollum, S. Jockusch and C. E. Crespo-Hernández, *Phys. Chem. Chem. Phys.*, 2015, **17**, 27851–27861.
12 B.-B. Xie, Q. Wang, W.-W. Guo and G. Cui, *Phys. Chem. Chem. Phys.*, 2017, **19**, 7689–7698.
13 S. Mai, M. Pollum, L. Martínez-Fernández, N. Dunn, P. Marquetand, I. Corral, C. E. Crespo-Hernández and L. González, *Nat. Commun.*, 2016, **7**, 13077.
14 L. Martínez-Fernández, G. Granucci, M. Pollum, C. E. Crespo-Hernández, M. Persico and I. Corral, *Chem. – Eur. J.*, 2017, **23**, 2619–2627.
15 S. Mai, P. Marquetand and L. González, *J. Phys. Chem. Lett.*, 2016, **7**, 1978–1983.
16 S. Mai, P. Marquetand and L. González, *J. Phys. Chem. A*, 2015, **119**, 9524–9533.
17 M. Ruckenbauer, S. Mai, P. Marquetand and L. González, *J. Chem. Phys.*, 2016, **144**, 074303.
18 S. Bai and M. Barbatti, *J. Phys. Chem. A*, 2016, **120**, 6342–6350.
19 M. Shukla and J. Leszczynski, *J. Phys. Chem. A*, 2004, **108**, 10367–10375.
20 O. Reelfs, P. Karran and A. R. Young, *Photochem. Photobiol. Sci.*, 2012, **11**, 148–154.
21 A. Favre, C. Saintomé, J.-L. Fourrey, P. Clivio and P. Laugâa, *J. Photochem. Photobiol., B*, 1998, **42**, 109–124.
22 J. A. Sanchez-Rodriguez, A. Mohamadzade, S. Mai, B. Ashwood, M. Pollum, P. Marquetand, L. Gonzalez, C. E. Crespo-Hernandez and S. Ullrich, *Phys. Chem. Chem. Phys.*, 2017, **19**, 19756–19766.
23 A. Mohamadzade, S. Bai, M. Barbatti and S. Ullrich, *Chem. Phys.*, 2018, **515**, 572–579.
24 S. Mai, A. Mohamadzade, P. Marquetand, L. González and S. Ullrich, *Molecules*, 2018, **23**, 2836.
25 H. Yu, J. A. Sanchez-Rodriguez, M. Pollum, C. E. Crespo-Hernández, S. Mai, P. Marquetand, L. González and S. Ullrich, *Phys. Chem. Chem. Phys.*, 2016, **18**, 20168–20176.
26 C. T. Middleton, K. de La Harpe, C. Su, Y. K. Law, C. E. Crespo-Hernández and B. Kohler, *Annu. Rev. Phys. Chem.*, 2009, **60**, 217–239.
27 C. E. Crespo-Hernández, B. Cohen, P. M. Hare and B. Kohler, *Chem. Rev.*, 2004, **104**, 1977–2020.
28 J.-M. L. Pecourt, J. Peon and B. Kohler, *J. Am. Chem. Soc.*, 2000, **122**, 9348–9349.
29 C. Reichardt and C. E. Crespo-Hernández, *J. Phys. Chem. Lett.*, 2010, **1**, 2239–2243.
30 M. Pollum and C. E. Crespo-Hernández, *J. Chem. Phys.*, 2014, **140**, 071101.

 

31 B. Ashwood, S. Jockusch and C. E. Crespo-Hernández, *Molecules*, 2017, **22**, 379.
32 D. Koyama, M. J. Milner and A. J. Orr-Ewing, *J. Phys. Chem. B*, 2017, **121**, 9274–9280.
33 J. Jiang, T.-s. Zhang, J.-d. Xue, X. Zheng, G. Cui and W.-h. Fang, *J. Chem. Phys.*, 2015, **143**, 11B605.
34 L. Martinez-Fernandez, T. Fahleson, P. Norman, F. Santoro, S. Coriani and R. Improta, *Photochem. Photobiol. Sci.*, 2017, **16**, 1415–1423.
35 G. Cui and W.-h. Fang, *J. Chem. Phys.*, 2013, **138**, 044315.
36 J. P. Gobbo and A. C. Borin, *Comput. Theor. Chem.*, 2014, **1040**, 195–201.
37 C. Reichardt and C. E. Crespo-Hernández, *Chem. Commun.*, 2010, **46**, 5963–5965.
38 O. Ghafur, S. W. Crane, M. Ryszka, J. Bockova, A. Rebelo, L. Saalbach, S. De Camillis, J. B. Greenwood, S. Eden and D. Townsend, *J. Chem. Phys.*, 2018, **149**, 034301.
39 R. Borrego-Varillas, D. C. Teles-Ferreira, A. Nenov, I. Conti, L. Ganzer, C. Manzoni, M. Garavelli, A. Maria de Paula and G. Cerullo, *J. Am. Chem. Soc.*, 2018, **140**, 16087–16093.
40 N. L. Evans and S. Ullrich, *J. Phys. Chem. A*, 2010, **114**, 11225–11230.
41 H. Yu, N. L. Evans, V. G. Stavros and S. Ullrich, *Phys. Chem. Chem. Phys.*, 2012, **14**, 6266–6272.
42 N. L. Evans, H. Yu, G. M. Roberts, V. G. Stavros and S. Ullrich, *Phys. Chem. Chem. Phys.*, 2012, **14**, 10401–10409.
43 D. Holland, M. MacDonald, M. Hayes, P. Baltzer, B. Wannberg, M. Lundqvist, L. Karlsson and W. Von Niessen, *J. Phys. B: At., Mol. Opt. Phys.*, 1996, **29**, 3091.
44 J. Leszczynski and K. Lammertsma, *J. Phys. Chem.*, 1991, **95**, 3128–3132.
45 A. Nenov, I. Conti, R. Borrego-Varillas, G. Cerullo and M. Garavelli, *Chem. Phys.*, 2018, **515**, 643–653.
46 J. Pople and R. K. Nesbet, *J. Chem. Phys.*, 1954, **22**, 571–572.
47 M. W. Schmidt, K. K. Baldridge, J. A. Boatz, S. T. Elbert, M. S. Gordon, J. H. Jensen, S. Koseki, N. Matsunaga, K. A. Nguyen and S. Su, *J. Comput. Chem.*, 1993, **14**, 1347–1363.
48 M. S. Gordon and M. W. Schmidt, *Theory and applications of computational chemistry*, Elsevier, 2005, pp. 1167–1189.
49 Y.-C. Jin and X.-M. Zheng, *Acta Phys.-Chim. Sin.*, 2017, **33**, 1989–1997.
50 D. C. Teles-Ferreira, I. Conti, R. Borrego-Varillas, A. Nenov, I. H. Van Stokkum, L. Ganzer, C. Manzoni, A. M. de Paula, G. Cerullo and M. Garavelli, *Chem. – Eur. J.*, 2020, **26**, 336–343.
51 H. R. Hudock, B. G. Levine, A. L. Thompson, H. Satzger, D. Townsend, N. Gador, S. Ullrich, A. Stolow and T. J. Martinez, *J. Phys. Chem. A*, 2007, **111**, 8500–8508.
52 M. El-Sayed, *J. Chem. Phys.*, 1963, **38**, 2834–2838.
53 M. A. Manae and A. Hazra, *J. Phys. Chem. A*, 2019, **123**, 10862–10867.